IEEE Open Journal of
Intelligent Transportation
Systems

Received 17 April 2023; revised 1 July 2023; accepted 31 August 2023. Date of publication 8 September 2023; date of current version 22 September 2023.

Digital Object Identifier 10.1109/OJITS.2023.3312660

Extrinsic and Temporal Calibration of Automotive Radar and 3-D LiDAR in Factory and On-Road Calibration Settings

CHIA-LE LEE[1], CHUN-YU HOU[1], CHIEH-CHIH WANG[2,3] (Member, IEEE), AND WEN-CHIEH LIN[4]

[1]Institute of Electrical and Computer Engineering, National Yang Ming Chiao Tung University, Hsinchu 300, Taiwan

[2]Department of Electrical and Computer Engineering, National Yang Ming Chiao Tung University, Hsinchu 300, Taiwan

[3]Mechanical and Mechatronics Systems Research Laboratories, Industrial Technology Research Institute, Hsinchu 31040, Taiwan

[4]Department of Computer Science, National Yang Ming Chiao Tung University, Hsinchu 300, Taiwan

CORRESPONDING AUTHOR: C.-C. WANG (e-mail: bobwang@ieee.org)

This article has supplementary downloadable material available at https://doi.org/10.1109/OJITS.2023.3312660, provided by the authors.

ABSTRACT While automotive radars are widely used in ADAS and autonomous driving, extrinsic and temporal calibration of automotive radars with other sensors is still daunting due to the sparsity, uncertainty, and missing elevation angles of automotive radar measurements. We propose a target-based calibration approach of 3D automotive radar and 3D LiDAR that performs extrinsic and temporal calibration in both factory and on-road settings. In factory calibration settings, a map is built with precise target poses; target trajectories are estimated based on map-based target localization in which the accuracy of both nearby and faraway target pose estimates can be ensured. The spatial and temporal relationships between radar and LiDAR measurements are established with target trajectories to accomplish extrinsic and temporal calibration. The proposed data collection procedure provides sufficient motion for analyzing time delay between sensors and can significantly reduce the data collection effort and time. There is 52.3% distance error reduction after time delay compensation in the experiment, which shows the improvements of temporal calibration. In on-road calibration settings, the metal objects with semantic labels, such as traffic signs, are selected as calibration targets. Although there could be insufficient correspondences to infer the missing dimension of planar radar for six DoF extrinsic calibration as demonstrated in factory calibration settings, the three extrinsic parameters and the time delay are shown still to be accurate. We validated the proposed method using the nuScenes datasets, which provide sensor measurements, poses, and HD map. With twenty-two data logs, each has over 1000 correspondences, the result of extrinsic parameters reaches centimeter-level accuracy compared with the offered benchmark. The time delay compensation improves 1 meter error for radar tracking in a 20 m/s vehicle case and improves mapping quality in real world data.

INDEX TERMS Radar, LiDAR, extrinsic calibration, temporal calibration.

I. INTRODUCTION

MACHINE perception in assisted and autonomous driving is critical. Sensor fusion is capable of ensuring and improving the performance and reliability of machine perception modules. Among various kinds of sensors, radars and LiDARs are widely used for sensor fusion. A LiDAR can offer dense environment measurements which could often be degraded in adverse weather conditions. On the other hand, an automotive radar provides sparse detection points with radial velocities, which would not be influenced by weather such as rain, fog, and snow.

Sensor calibration is a fundamental and critical procedure for sensor fusion. Precise calibration enables the fusion of

The review of this article was arranged by Associate Editor Pardis Khayyer.

FIGURE 1. Sensor rack on the test vehicle equipped with a Velodyne HDL-32E LiDAR and a Delphi ESR radar.

sensor data from multiple sources, leading to higher-level perception and more robust autonomous systems [1], [2]. There have been a number of studies on calibration between LiDARs, cameras or IMUs [3], [4], [5], [6], [7], [8], [9], [10]. Although automotive radars are widely used in self-driving vehicles, very few works in the literature address the radar-LiDAR calibration [11], [12]. While calibration could include intrinsic, extrinsic, and temporal calibration, we focus on extrinsic and temporal calibration and assume that intrinsic calibration is accomplished by the sensor manufacturers. In this paper, we propose a novel method to perform extrinsic and temporal calibration between an automotive radar and a 3D LiDAR that can adapt in both factory and online settings. Fig. 1 shows the test vehicle equipped with the sensors used in this work. In addition, the nuScenes open datasets [13] are used for verifying the proposed approach in the on-road settings.

In the nuScenes datasets, we observe that radar has around 0.05 second time delay, which can causes one meter error for a vehicle at 20 m/s speed which could be severe on safety. Most of the recent works [3], [4], [5], [6], [7], [8], [9], [10] on temporal calibration between camera, LiDAR or IMU are based on sensor motion alignment, which aligns the estimated motions of different sensors to infer the time delay between the sensors. The performance of these calibration approaches highly depends on the accuracy of sensor motion estimation. However, when the calibration involves a radar, these approaches could not perform well as the estimation of radar motion is not accurate enough due to the sparseness and uncertainty of radar measurements. Accordingly, we apply a target trajectory alignment approach in this work. Owing to the uncertainty of radar measurements, rapid velocity of the target relative to the radar and LiDAR sensors is preferred during data collection for ensuring the time delay's observability. In our previous work [14], the long range targets with planar automotive radar's yaw rotation motion is used to magnify time delay effects. The LiDAR target localization method is proposed to deal with the sparse LiDAR measurements in far range.

In this work, we propose an algorithm and a data collection procedure that can calculate extrinsic and temporal calibration parameters in both factory and on-road scenarios. The general idea of the proposed method is to leverage a target trajectory alignment approach to enable extrinsic and temporal calibration between automotive radar and 3D LiDAR sensors. The proposed method effectively deals with sparse LiDAR measurements at a far range by utilizing a LiDAR target localization method. Our approach is designed to be adaptable for both factory settings and on-road scenarios. For factory calibration, a pre-built map of the calibration environment, designed targets, and specific motion generation of the sensor rack are required to establish correspondence and generate sufficient deviation for calibration. While on-road calibration could be essential for calibration parameter deviation diagnosis on daily operations of self-driving vehicles, the proposed method can also accomplish on-road calibration with sensor measurements, pre-selected targets, and a pre-built map. Due to the state-of-the-art (SOTA) LiDAR-based detectors have low accuracy for faraway objects [15], the proposed target localization method (Section III-C) would be more suitable for on-road calibration. The proposed on-road calibration method is validated on the nuScenes dataset [13]. It provides LiDAR and radar measurements with annotation and metadata including calibration, maps, vehicle coordinates, etc. The nuScenes Boston dataset is chosen for on-road calibration and the result compared with offered calibration benchmark. For the target selection, traffic lights are chosen as pre-selected targets in this work, which could be stably measured by automotive radars. The target locations are estimated with the maps and the vehicle pose estimates from LiDAR-based localization.

Notice that only 3 DoF extrinsic parameters and time delay can be estimated with limited targets candidates in on-road scenarios due to a lack of the radar cross-section (RCS)-elevation dependence which is required to infer the missing dimension in 6 DoF extrinsic calibration in Peršić et al. [11], [12]. Although there are more interference and restrictions in on-road scenarios, the estimated extrinsic parameter reaches centimeter-level accuracy. Comparing to the offered benchmark, the errors are under 0.08 meter and 0.03 degree. The estimated time delay is 0.05 s and the improvement on time delay compensation is also validated on fundamental autonomous driving modules such as mapping and object tracking in Section V.

This paper is based on our previous work [14], where the LiDAR target localization for calibration and the approach of 3D LiDAR–radar temporal calibration were presented. We extend our work with three novel contributions. Firstly, we proposed an efficient data collection approach that streamlines the calibration procedure. Sufficient yaw and pitch motions are directly applied to the sensors in which correspondences across radar horizontal and vertical FoV are established for obtaining RCS-elevation dependence. This simplifies the data collection procedure from a day of work to an hour process. Secondly, since motion is generated in the data collection procedure, the time delay estimation is combined into the reprojection error minimization stage. Thirdly, we present an on-road calibration solution, which is

distinct from our previous work. This solution addresses the challenge of calibrating LiDAR and radar systems in real-world driving scenarios. We demonstrate the effectiveness of our approach through on-road experiments and showcase the improvements with downstream tasks, including object tracking and mappings. The core contribution of this paper is not just the proposal to attain extrinsic and temporal calibration between radar and LiDAR. It's also about proving the effectiveness under laboratory conditions as well as on-road scenarios.

II. RELATED WORK

The extrinsic calibration methods can be categorized as target-based or target-less, online or offline, depending on the characteristics of sensors and application scenarios. Besides, motion-alignment based approaches are applied for temporal calibration since the effects of time delay could be only observable when a sufficient motion is applied to the sensors or calibration targets. In this section, the related research on extrinsic and temporal calibrations of radar and LiDAR is discussed.

A. RADAR-RELATED EXTRINSIC CALIBRATION

For studies on radar-related extrinsic calibration, most studies focus on calibration between radar and camera. Since metal materials are easily detected by radar, metal objects are often used as targets. For instance, a metal panel is used to estimate a 3×3 homography matrix mapping the radar measurements into the camera image plane [16]. A more common choice is corner reflectors as its specific design ensures the reflected waves to propagate along their incident direction and return to their source, i.e., corner reflectors can provide reliable measurements with higher RCS values comparing with other objects. Sugimoto et al. [17] move the corner reflector up and down to find the measurements with local maximum in intensities and use these measurements to optimize a homography transformation matrix.

While the aforementioned radar calibration approaches provided decent results, these approaches could not accomplish full six degrees of freedom (6-DoFs) extrinsic calibration between radar and camera. The main reason is that planar automotive radars only provide two-dimensional measurements while missing the elevation information. This causes the main difficulty in estimating accurate 6-DoF extrinsic parameters between automotive planar radars and other sensors. To solve this issue, Peršić et al. [11], [12] use RCS values to infer the missing dimension of the planar radar because the RCS values vary with the elevation angles. In [11], the radar's nominal FoV in the LiDAR data is fitted by encompassing as many measurements with high RCS values as possible. The RCS value distribution across radar's vertical FoV is modelled as a curve function of the elevation of the target [12]. An accurate 6-DoF transformation between radar and LiDAR, or between radar and camera can then be estimated.

More recently, with the emergence of 4D radars, a number of approaches utilize the additional elevation information to calibrate the 6-DoF extrinsic parameters between 4D radar and LiDAR. Heng [18] proposes a 6-DoF target-less calibration method by optimizing point-to-plane distances between radar scans and a 3D map. Using 4D radar velocity measurements, Wise et al. [19] also propose a target-less calibration approach which minimizes the errors between the radar velocity measurements and the motion of other sensors. Although these approaches can accomplish 6-DoF calibration with fewer restrictions, it is still challenging to calibrate planar automotive radars, which are still more widely used in autonomous vehicles currently.

B. LIDAR-RELATED EXTRINSIC CALIBRATION

There have been extensive research on LiDAR-camera calibration in which using specific designed target is a common choice. For instance, [20] used multiple planar checkerboard patterns to perform calibration in a single shot. A white polygonal planar board was used in [21] since the board is easier to be perceived by camera and LiDAR. In order to estimate the targets' 3D poses from images, ArUco tags are used in [22]. The ArUco tags are printed on the rectangular boards such that LiDAR can perceive the targets as well. 3D-3D correspondences in LiDAR and camera measurements can be established accordingly. A planar target with four circular holes is used in which the centers of four circular holes can be estimated through LiDAR point cloud and stereo point cloud [23]. Contrary to target-based approaches, some research focuses on using the features from outdoor environments. In [24], [25], calibration is completed via data alignment of laser depth and image edges of outdoor environments. Besides, road markings can also be used for the optimization of extrinsic parameters [26]. Since these approaches use environment features, they could be implemented as online/on-road calibration.

Compared with calibration between LiDAR and camera, there are fewer works on LiDAR-IMU calibration. The method in [27] is able to estimate 6 DoF extrinsic parameters between LiDAR and IMU as it uses room corners as target. In [28], a trajectory based hand-eye calibration method is proposed in which both large and small trajectories are used to estimate the rotation and translation respectively.

C. TEMPORAL CALIBRATION

Most of the recent works on temporal calibration between cameras, LiDAR or IMU are target-less, motion-alignment based approaches [3], [4], [5], [6], [7], [8], [9], [10]. Following the same motion-alignment principles, we present an approach to accomplish temporal calibration of automotive radar and 3D LiDAR. Since the motion and the trajectory estimation using radar are less accurate compared to LiDAR, camera, and IMU, a target-based, trajectory-alignment approach is proposed in this work.

Specifically for the field of automotive radar and 3D LiDAR calibration, Peršić et al. [11], [12] used RCS values

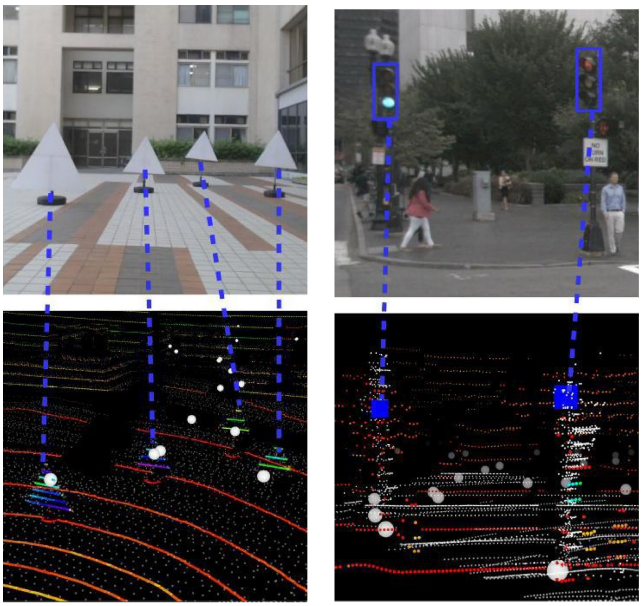

(a) Factory setting (b) On-road setting

FIGURE 2. The targets in the experiment area. The objects which have stable radar measurements are chosen as targets.

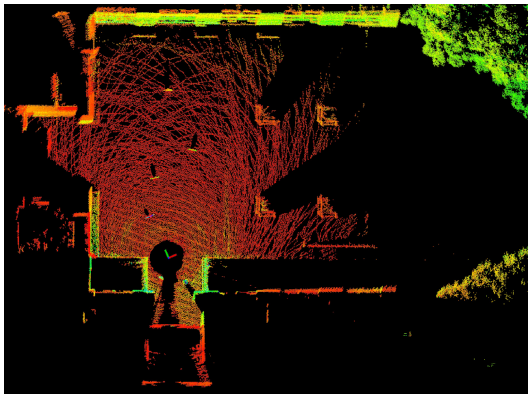

FIGURE 3. Point cloud map of experiment environment.

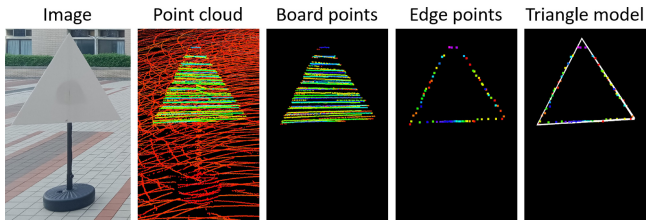

FIGURE 4. Triangle Model-fitting.

to infer the missing dimension of the automotive radar to achieve 6-DoF extrinsic calibration. However, they only addressed the extrinsic calibration of radar LiDAR calibration. Our previous work [14] addressed both extrinsic and temporal calibration problems of automotive radar and LiDAR with two-stage optimization and validated the effectiveness of the method in terms of both extrinsic and temporal calibration compared to [11], [12]. We extend our work with a simplified data collection approach, incorporating extrinsic and temporal calibration into one stage, and on-road calibration solution.

III. SENSORS CORRESPONDENCE ESTABLISHMENT

The proposed method is a target-based calibration in which targets are used to establish the spatial and temporal relationships between radar and LiDAR. With the established correspondences, the spatial transformation and the temporal delay between sensors can be estimated.

The target designed in factory-setting experiments follows [11], [12] which combines a corner reflector and a triangular styrofoam board for radar and LiDAR detection respectively as shown in Fig. 2(a). The proposed on-road calibration system follows the same approach to establish the correspondence with a given semantic map. The metal material objects, e.g., traffic light and traffic sign as shown in Fig. 2(b) which can be stably measured by radar are suitable as pre-selected targets without placing additional targets on roads.

A. ESTIMATING THE TARGET CENTER FROM THE LIDAR MEASUREMENTS

Although LiDAR can provide dense 3D point measurements, the measurements could still become sparse for long-range objects, resulting in the accuracy decrease of target center estimation. Following our earlier work [14], rather than estimating the target center directly, the target center is estimated via LiDAR localization in which the target pose is given in the pre-built map. By doing so, the centers of long-range targets can be estimated more precisely, and the overlap of FoV between radar and LiDAR is not necessary. In the data collection process, it is only necessary to ensure the targets can be perceived by radar. The approach is divided into two steps.

1) MAPPING AND LOCALIZATION

A point cloud map of the experiment environment can be built as shown in Fig. 3 by using the existing SLAM algorithms/systems. And the transformation ${}^{l}T_{m}(t_j)$ from the map frame to the LiDAR frame at time t_j can be estimated via LiDAR-based localization, e.g., Iterative Closest Point (ICP) [29] and Normal Distribution Transform (NDT) [30].

2) ESTIMATION OF THE TARGET CENTER

By simply transforming poses of target centers from the map frame F_m to the LiDAR frame F_l, the target centers at each LiDAR scan are computed. For factory setting experiment, a triangle model is defined and optimized to fit the edge points of the board for each target to estimate the target pose in the map as shown in Fig. 4. We extract the edge points from the LiDAR measurements by using geometric and intensity information and adapt triangle model fitting to estimate the accurate target pose in the pre-built map [14]. For on-road setting experiments, rather than detecting target center directly, it would be more suitable and accurate to

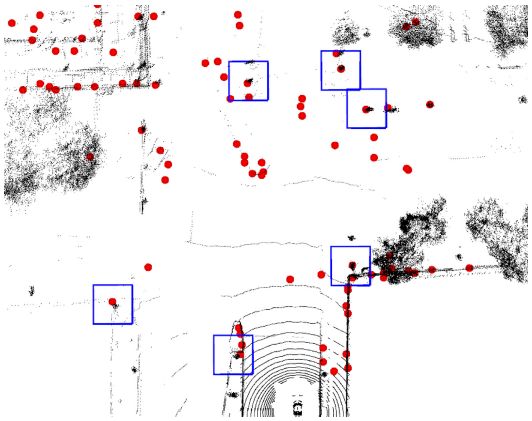

FIGURE 5. The closest measurement of the searching region is selected as a target candidate. Black point: LiDAR map and LiDAR scan; red point: radar measurement; blue box: searching regions where targets are at the centers of the regions.

obtain target pose from the offered semantic map. The radar observability should be considered while selecting the type of target.

We denote the position of the k-th target in the map as ${}^{m}p_{lk}$, and the target center in the LiDAR frame ${}^{l}p_{lk}$ at time t_j can be estimated by the following equation:

$$ {}^{l}p_{lk}(t_j) = {}^{l}T_m(t_j)\,{}^{m}p_{lk}. \tag{1} $$

B. ESTIMATING THE TARGET CENTER FROM THE RADAR MEASUREMENTS

A radar measurement includes the measured range ${}^{r}r_r$, azimuth angle ${}^{r}\phi_r$, and RCS value δ_r, where the left superscript represents a measurement resides at the radar frame F_r and the right subscript means the measurement is measured from the radar. Since most automotive radars do not provide vertical information for measurements (i.e., the elevation angle is missing), there is a potential arc in which the measured object can reside in 3D space for each radar measurement. For most radar applications, the projected point on the radar plane P_r (of elevation angle equals 0) is often used as the position of an object. However, the missing elevation angles would cause a non-negligible estimation error when calibrating an automotive radar with other sensors. Nevertheless, the missing components such as z-translation, pitch, and roll, can still be refined by RCS values. The details will be discussed in Section IV-B.

Compared to LiDARs, there could be insufficient object structure information from radar measurements and it could be difficult to extract targets directly from radar measurements. With LiDAR target center estimation and an initial approximate transformation, possible target location regions are speculated. We select radar measurements which are closest to the centers of these regions as targets as shown in Fig. 5 and track the targets during the data collection process. At time t_i the target center estimation of the k-th target: ${}^{r}s_{rk}(t_i) = [{}^{r}r_{rk}(t_i) {}^{r}\phi_{rk}(t_i)]$ with the RCS value $\delta_{rk}(t_i)$ can be collected for extrinsic and temporal calibration. The details will be discussed in Section III-C.

C. CORRESPONDENCE ESTABLISHMENT

To associate the data from the automotive Radar and LiDAR, the target centers estimated from LiDAR are transformed into the radar frame by an initial approximate transformation ${}^{r}T_l$.

We follow the two-step optimization proposed by Peršić et al. [12]. The transformation ${}^{r}T_l$ from F_l to F_r includes two parts: $[{}^{r}t_l^{l}\Theta_r]$, where ${}^{r}t_l = [t_x\ t_y\ t_z]$ and ${}^{l}\Theta_r = [\theta_z\ \theta_y\ \theta_x]$ denote the translation part from F_l to F_r, and rotation part from F_r to F_l. The Euler angle representation is used in the rotation part ${}^{l}\Theta_r$, where θ_z, θ_y, θ_x are yaw, pitch and roll, and the rotation matrix R is given by:

$$ R\left({}^{l}\Theta_r\right) = R_x(\theta_x)R_y(\theta_y)R_z(\theta_z) \tag{2} $$

where R_x, R_y, R_z are the rotation matrix along x, y, z axis respectively. The target center ${}^{l}p_{lk}(t_j)$ estimated from LiDAR is transformed to the radar frame as ${}^{r}p_{lk}(t_j)$:

$$ {}^{r}p_{lk}(t_j) = {}^{r}T_l\ {}^{l}p_{lk}(t_j) = R\left({}^{l}\Theta_r\right)^{T}\ {}^{l}p_{lk}(t_j) + {}^{r}t_l \tag{3} $$

The radar measurements which are closest to ${}^{r}p_{lk}(t_j)$ and within a predefined distance threshold is chosen as the target center estimates. Since the target centers estimation from radar is described in the spherical coordinate system, ${}^{r}p_{lk}(t_j)$ is converted to the representation in spherical coordinate as ${}^{r}s_{lk}(t_j) = [{}^{r}r_{lk}(t_j) {}^{r}\phi_{lk}(t_j) {}^{r}\psi_{lk}(t_j)]$ for reprojection process in Section IV-A. In addition, linear interpolation [31] is used to compensate for timestamp differences. It should be noted that uncertainties in the map and the localization module could degrade the performance of LiDAR target center estimation. The accuracy of the map and the localization approaches should be analyzed and could be further improved to obtain better calibration results. Once the correspondences between radar and LiDAR measurements are established, extrinsic and temporal calibration could be accomplished using these correspondences.

IV. EXTRINSIC AND TEMPORAL CALIBRATION

In our previous work [14], we follow the two-stage optimization procedure proposed by [11], [12], which include the reprojection error minimization and RCS optimization to accomplish extrinsic calibration, and then perform the temporal calibration stage. According to the proposed data collection method which contains rapid sensor motions, the time delay effects should be directly considered. In this work, the time delay is optimized in the reprojection error minimization stage. The time delay effects on the extrinsic parameters are analyzed in Section V-A.

Since the on-road measurements do not contain sufficient RCS-elevation dependence (see Section V-B), the RCS optimization stage is not performed in on-road calibration. On-road calibration only performs reprojection error minimization to estimate 3 DoF extrinsic parameters and time delay. We propose an iterative procedure for on-road calibration and the flow chart is shown in Fig. 6 More detail will be discussed in Section V-B.

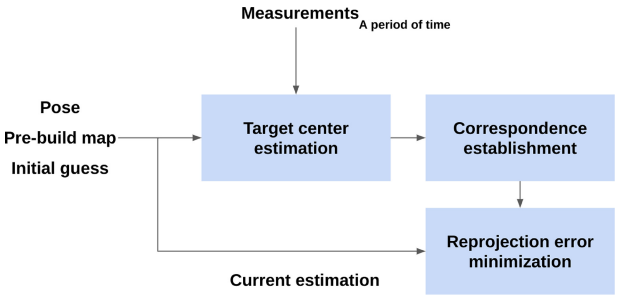

FIGURE 6. The flow chart of the on-road calibration implementation.

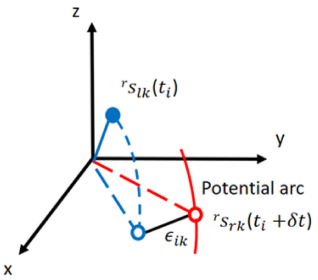

FIGURE 7. Reprojection error (ϵ_{ik}). Blue filled circle: k-th LiDAR target in radar frame at time t_i($^r s_{lk}(t_i)$); blue hollow circle: the projection of LiDAR target; red hollow circle: the projection of k-th radar target in radar frame at time $t_i + \delta t$($^r s_{rk}(t_i + \delta t)$).

A. REPROJECTION ERROR MINIMIZATION

The 6 DoF extrinsic parameters are represented as a parameter set $c_p = [{}^r t_l^T \Theta_r]$. Accordingly, the LiDAR data ${}^r s_{lk}(t_i) = [{}^r r_{lk}(t_i) {}^r\phi_{lk}(t_i) {}^r\psi_{lk}(t_i)]$ for each correspondence can be obtained, and projected into the radar plane by ignoring the elevation angle ${}^r\psi_{l,i}$. Considering the time delay term, we assume the time delay between radar and LiDAR is a constant time δt and each radar data would be compensated.

Therefore, the reprojection error term ϵ_{ik} is defined as the distance between the projected LiDAR data and compensated radar data on the radar plane in which ${}^r\psi_{lk}(t_i) = {}^r\psi_{rk}(t_i + \delta t) = 0°$ as shown in Fig. 7.

$$\epsilon_{ik}(c_p, \delta t) = \left\| \begin{bmatrix} {}^r r_{lk}(t_i) \cos({}^r\phi_{lk}(t_i)) \\ {}^r r_{lk}(t_i) \sin({}^r\phi_{lk}(t_i)) \end{bmatrix} - \begin{bmatrix} {}^r r_{rk}(t_i + \delta t) \cos({}^r\phi_{rk}(t_i + \delta t)) \\ {}^r r_{rk}(t_i + \delta t) \sin({}^r\phi_{rk}(t_i + \delta t)) \end{bmatrix} \right\| \quad (4)$$

The calibration parameters $\hat{c_p}, \hat{\delta t}$ are obtained by minimizing the cost function using the Levenberg-Marquardt (LM) algorithm implemented by the Ceres Solver [32]:

$$\hat{c_p}, \hat{\delta t} = \arg\min_{c_p, \delta t} \left(\sum_{i=0}^{N-1} \sum_{k=0}^{K-1} \epsilon_{ik}^2 \right) \quad (5)$$

The cost function is the sum of the squares of the reprojection error across $N \times K$ correspondences. N is the number of LiDAR scans, K is the number of calibration targets.

B. RCS OPTIMIZATION

Once the reprojection error minimization is completed, the six calibration parameters are estimated. However, t_z, θ_y, θ_x would have higher uncertainty comparing with other parameters since the elevation angles of measurements are neglected in the projection process. Consequently, these three parameters are refined in the stage of the RCS optimization.

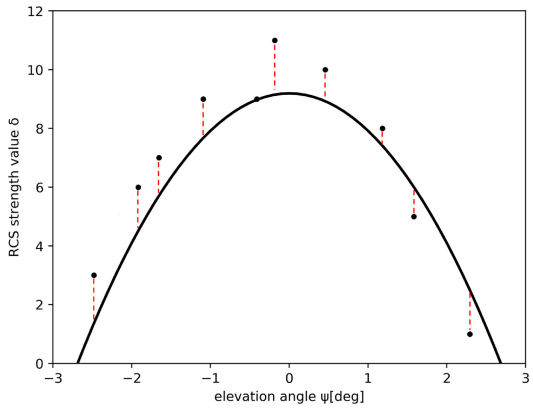

FIGURE 8. The demonstration of RCS error. Black point: measured RCS value; black line: expected RCS value from estimated RCS-elevation dependence; red dash line: RCS error.

Since a radar emits the largest amount of radiation at the zero elevation angle, the RCS measurements should be dependent on the elevation angle of the target. Following Peršić et al. [12], the RCS-elevation dependence can be modelled as a curve where the expected RCS value is defined as:

$$\hat{\delta}_l(t_i) = c_2 \cdot {}^r\psi_l(t_i)^2 + c_0, \quad (6)$$

where c_0, c_2 are the curve parameters. Accordingly, the RCS optimization parameter set consists of a subset of extrinsic parameters and curve parameters: $c_\delta = [t_z \ \theta_y \ \theta_x \ c_0 \ c_2]$. Fig. 8 shows the meaning of the RCS error term which is defined as the expected RCS value $\hat{\delta}_l$ and the measured RCS value δ_r:

$$\varepsilon_i(c_\delta) = \hat{\delta}_l(t_i) - \delta_r(t_i) \quad (7)$$

The cost function is defined as the sum of squares of RCS error and the parameter set $\hat{c_\delta}$ is obtained by minimizing the cost function using the Ceres Solver [32]:

$$\hat{c_\delta} = \arg\min_{c_\delta} \left(\sum_{i=0}^{N-1} \varepsilon_i(c_\delta)^2 \right). \quad (8)$$

V. EXPERIMENTS

The proposed calibration method is verified with both our datasets collected in a factory calibration setting and the nuScenes open datasets in on-road calibration settings.

A. FACTORY CALIBRATION

The factory calibration section is divided into four parts: the experiment setups, the target setups, the motion generation, and the factory calibration results. Since reprojection error minimization and RCS optimization are based on different optimization criteria, different target setups and motion generation method are used and described respectively.

FIGURE 9. The targets are placed in an open area. Multiple targets are used to collect more target measurements and accelerate the calibration process.

1) EXPERIMENT SETUPS

The sensors we use were the Velodyne HDL-32E 3D-LiDAR and the Delphi ESR V9.21.15 radar whose frequencies are 10 Hz and 20 Hz respectively. The sensor rack equipped with sensors can collect data easily, and can be placed on the top of a vehicle after calibration as shown in Fig. 1.

Since the used Delphi radar does not offer timestamp for each measurement, we generate the measurement timestamps from both sensors according to the computer's system clock in our data collection process. The addition delays would occur from communication, operating system, and Robot Operating System (ROS) and we assume those delays are summed to be a constant.

2) TARGET SETUPS

In this work, the target design follows our previous work [14]. The plastic materials which has low radar echo intensity is used to build the target stand. Thus, the actual target positions could be estimated by radar RCS thresholding. We choose the corner reflectors with 0.2 m side length. The corner reflectors are large enough to ensure the RCS values from the target are strong and distinguishable. Since the radar target center estimation would become unstable while other objects are close to targets in distance, the experiments were conducted in an uncluttered space as shown in Fig. 9.

For reprojection error minimization, the four targets are separately placed at ${}^{r}r_r = [5, 10, 15, 20]$ m, ${}^{r}\phi_r = [30, 15, -15, 0]^\circ$ initially, and ensured to be perceived by radars simultaneously. For RCS optimization, it is preferred that the targets are placed near and different azimuth angles to ensure the stability and observability of RCS measurements. The three targets are placed at ${}^{r}r_r = [5, 10, 10]$ m, ${}^{r}\phi_r = [0, -30, +30]^\circ$ and adjusted to point towards radar initially.

3) MOTION GENERATION

For reporjection error optimization, we give the sensors an yaw motion to obtain wide measurements distribution across radar horizontal FoV efficiently. Since the time delay would influence extrinsic calibration results due to motion, the time delay is also optimized in the reprojection error minimization stage. According to our previous work [14], the rapid motion of sensors is required for ensuring the accuracy of time delay estimation. To confirm this statement, a simulation generated based on experiments and target settings is performed in which noise components according to the specifications of radars and LiDARs are added. The simulated measurements are generated for 10000 runs with corresponding angular velocities of sensors in a fixed time period, 30 seconds. Table 1 shows the higher angular velocity, the lower error on time delay while other parameters are still estimated accurately. Accordingly, rapid motions of the sensor rack would be preferred to estimate time delay accurately. However, while a Velodyne LiDAR is used in this work, rapid motion would lead to a distortion in LiDAR measurements. Following our previous work, the rectification approach which compensates the motion is applied to resolve the distortion issue.

The RCS optimization is based on the observation that RCS measurements would have different value distributions across radar's vertical FoV. Thus, the correspondences at different elevation angles with respect to radar are required. In the previous studies [11], [12], [14], the targets are placed at different heights ranging from the ground level up to a 2 m height to meet the requirements. Instead, we give the radar a slow motion of pitch changes so as to acquire dense observations of target at different elevation angles efficiently as shown in Fig. 10. In practice, the motions are generated by two people who hold each side of the sensor rack. For each data collection task, the sensor rack is rotated to obtain the measurements distributing in the radar FOV as stable as possible (see the video in the supplemental materials).

TABLE 1. Simulation: The mean of error between estimated parameters and ground truth with different motion speed.

Angular Velocity [rad]	Δt_x [cm]		Δt_y [cm]		$\Delta\theta_z$ [°]		$\Delta\delta t$ [ms]	
	mean	std	mean	std	mean	std	mean	std
0.1	0.457	0.343	1.407	0.975	0.075	0.051	5.699	3.426
0.2	0.456	0.353	1.458	1.008	0.077	0.052	2.521	1.639
0.3	0.450	0.340	1.342	0.946	0.072	0.049	1.640	1.097
0.4	0.444	0.335	1.057	0.800	0.060	0.044	1.168	0.810
0.5	0.440	0.331	0.885	0.681	0.053	0.040	0.927	0.652

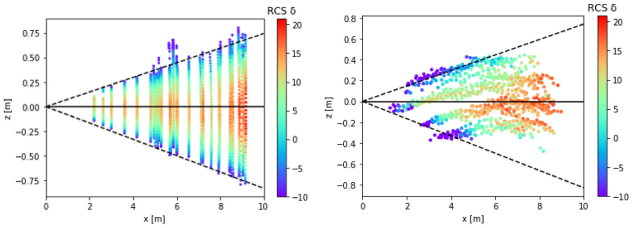

(a) Proposed method (b) Our previous work [14]

FIGURE 10. The comparison of the spatial distribution across transformed LiDAR data between the proposed method and our previous work which follows Peršić et al. [12]. Each correspondence is colored according to it RCS measurement. Black dash line: radar's vertical FoV.

TABLE 2. Monte Carlo analysis: Calibration result of two-stage optimization.

	Reprojection Error Minimization	RCS Optimization
$t_x[m]$	$N(-0.214, 4.956 \times 10^{-4})$	—
$t_y[m]$	$N(-0.001, 4.302 \times 10^{-4})$	—
$t_z[m]$	$N(1.010, 9.051 \times 10^{-2})$	$N(0.231, 4.629 \times 10^{-5})$
$\theta_z[^\circ]$	$N(32.708, 2.863 \times 10^{-2})$	—
$\theta_y[^\circ]$	$N(6.329, 4.835 \times 10^{-0})$	$N(1.427, 9.761 \times 10^{-3})$
$\theta_x[^\circ]$	$N(7.222, 5.487 \times 10^{-1})$	$N(-1.262, 1.681 \times 10^{-2})$
$\delta t[s]$	$N(-0.095, 2.779 \times 10^{-6})$	—

TABLE 3. Time delay effort analysis.

	Proposed	Previous [14] $\hat{\delta t}$ = 0	Previous [14] $\hat{\delta t}$ = -0.1	Tape measured
$t_x[m]$	-0.23	-0.245	-0.245	-0.22
$t_y[m]$	-0.02	-0.07	0	-0.03
$\theta_z[^\circ]$	32.96	33.712	32.653	—
$\delta t[s]$	-0.095	-0.093	-0.094	—

4) FACTORY CALIBRATION RESULTS

The two-stage optimization is accomplished and the calibration results for reprojection error minimization $\hat{c_p}$, $\hat{\delta t}$, RCS optimization $\hat{c_\delta}$, the tape measured translations ${}^r\tilde{t}_l$ are listed below:

- $\hat{c_p} = [-0.23\ m,\ -0.02\ m,\ +0.19\ m,\ 32.96^\circ, 1.053^\circ, 6.137^\circ]$
- $\hat{\delta t} = -0.095\ s$
- $\hat{c_\delta} = [+0.296\ m,\ +1.422^\circ,\ -1.256^\circ]$
- ${}^r\tilde{t}_l = [-0.22\ m,\ -0.03\ m,\ +0.27\ m]$

In this setting, the initial guess was set to be $[{}^r t_l, {}^l\Theta_r | \delta t] = [t_x,\ t_y,\ t_z,\ \theta_z,\ \theta_y,\ \theta_x |\ \delta t] = [0\ m,\ 0\ m,\ 0\ m,\ 0^\circ,\ 0^\circ,\ 0^\circ |\ 0\ s]$, where we used carefully tape measured translations and roughly adjusted θ_z such that the correspondences could be established as described in Section III-C. In our previous work [14], while time delay is estimated after extrinsic calibration, the data collection with slow motion is requested for extrinsic calibration to reduce the influence of the time delay. In Table 3, we analyze how the time delay influence the extrinsic parameters in the proposed data collection method. While considering the time delay and setting the initial guess to –0.1 s which is close to the estimated time delay, the previous method [14] would converge near the proposed method. However, while the time delay is ignored and set to 0 s, the θ_z has about 0.75° deviation to compensate the time delay effort according to the motion.

We also performed Monte Carlo experiments for 1000 runs by randomly sub-sampling all the correspondences into half of the original number. The results are fitted with a Gaussian distribution and the estimated parameters are shown in Table 2. In the reprojection error minimization stage, t_z, θ_y, θ_x have larger variances than other parameters. After RCS optimization, the variances of those three parameters are decreased significantly and the means are refined as well.

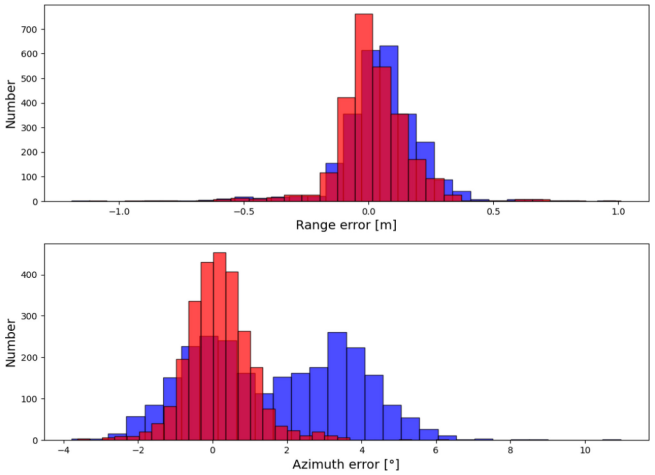

FIGURE 11. The distribution of range error and azimuth error. Blue: before reprojection error minimization; red: after reprojection error minimization.

It could be observed that there are slight differences between the estimated parameters in translation and the tape measurements. The differences could originate from the imprecision in tape measurements and the limits of accuracy in radar measurements ($\pm 0.25\ m$ for range accuracy; $\pm 1^\circ$ for azimuth accuracy [33]).

To assess the quality of the calibration results after reprojection error minimization, we examine the distribution of range errors $({}^r r_l - {}^r r_r)$ and azimuth errors $({}^r a_l - {}^r a_r)$ of all correspondences as shown in Fig. 11. The result shows that there are 93.2% correspondences with the range error within the range accuracy; 79.8% correspondences with the azimuth error within the azimuth accuracy which would make sense according to radar specification.

Given the spatial transformation estimated from reprojection error minimization, the performance of the temporal calibration is shown in Fig. 12. With the time delay compensation, the radar data are well aligned with transformed LiDAR data and the average reprojection error has 52.3% improvement in which the error is reduced from 0.35 m to 0.167 m.

For RCS Optimization, Fig. 13 shows the relation between the RCS value and the elevation angle ${}^r\psi_{lk}(t_i)$ of transformed LiDAR data. In contrast to the result in the reprojection error minimization stage, most target measurements are located outside radar's vertical FoV and have a symmetrical pattern across radar's elevation central after RCS value optimization.

B. ON-ROAD CALIBRATION

Comparing to the factory calibration, the on-road calibration performs in outdoor driving scenario in which there are more restrictions on targets and sensors motions. The purpose of on-road calibration could be to diagnose calibration parameters deviation and to offer a preliminary calibration. In detail, we use nuScences offered extrinsic parameters with

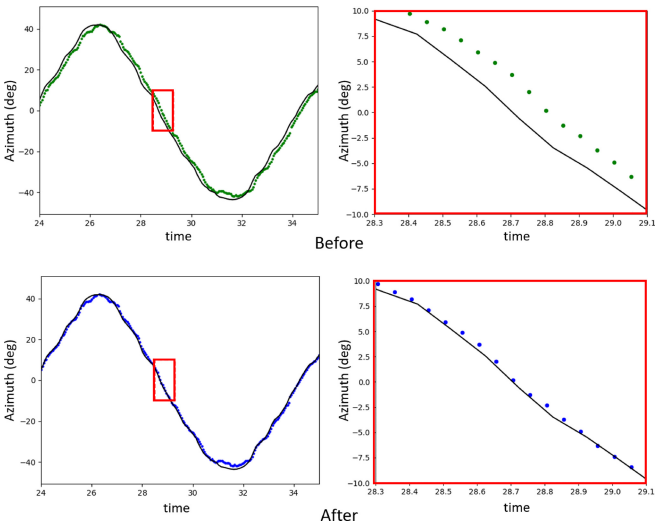

FIGURE 12. The comparison of time delay compensation at the target. Black curve: transformed LiDAR data; green points: radar data before temporal compensation; blue points: radar data after temporal compensation.

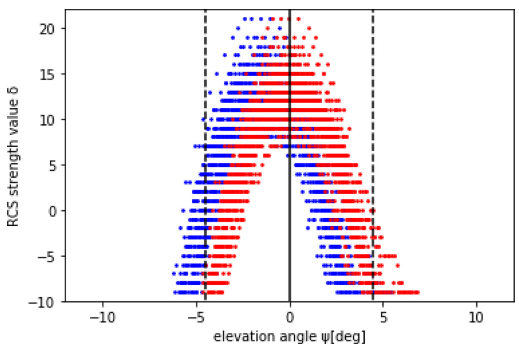

FIGURE 13. RCS distribution across the elevation angle of transformed LiDAR data. Blue points: before RCS optimization; red points: after RCS optimization; black dash line: radar's vertical FoV.

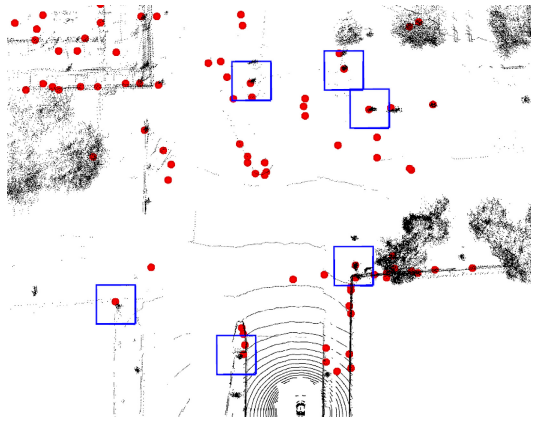

FIGURE 14. The demonstration of measurements and targets in on-road calibration. Black point: LiDAR map and LiDAR scan; red point: radar measurement; blue box: searching region where target at the center.

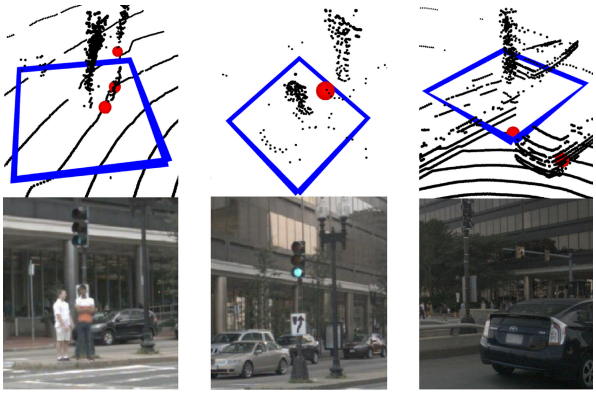

(a) Pedestrian (b) Pole (c) Vehicle

FIGURE 15. The interfering objects on road which would degrade the radar target estimation. Black point: LiDAR measurement; red point: radar measurement; blue box: searching regions where target at the center. (a) Pedestrian (b) Pole (c) Vehicle

addition bias and zero time delay as initial guess, pre-built semantic map, and vehicle pose to estimate the target center with measurements and establish the correspondences for a period of time in the beginning. The established correspondences are then used in reprojection error minimization to estimate extrinsic parameters and time delay. The result of this cycle would be treated as initial guess in the next cycle and this procedure would be iterated until the calibration parameters converge as shown in Fig. 6.

The nuScenes dataset [13] provides radar, LiDAR measurements, LiDAR pose and semantic maps in urban areas, which is suitable for verifying the performance of the proposed approach in on-road scenarios. In the categories of semantic map objects, traffic lights should be one of the best choices as pre-selected targets since traffic lights could be measured by radar steadily, as shown in Fig. 14.

However there are still other objects, such as pedestrian, pole and vehicle, which interfere the radar measurements as shown in Fig. 15, the calibration performance would decrease comparing to factory calibration settings. Since the target measurements provided by traffic sign are less accurate compared to reflector, extended Kalman filter (EKF) tracking is performed to refine the target trajectories. The LiDAR pose and traffic light annotation offered by nuScenes are used for LiDAR target center detection. It is observed that the RCS optimization would have low accuracy. It is shown that the RCS value and the target distance is not strongly correlated in Fig. 17 which does not follow the RCS-elevation dependence. Thus, RCS optimization does not involve in on-road calibration of the nuScenes datasets in this work.

Besides, it should be noted that the annotation of the traffic light is marked on the traffic light box, specifically. However, the traffic light's metal pole also provides firm radar measurement. This raised the concern of whether the radar measurement comes from the traffic light box or pole. We have inspected the structure of traffic lights in all experiments' data logs and concluded that there are two types of traffic light structures, as shown in Fig. 16. There is no disturbance for those traffic light boxes far from the pole (Fig. 16(a)). For the traffic light boxes close to the metal pole, we use extended Kalman filter (EKF) to track the

(a) Far (b) Near

FIGURE 16. The two types of traffic light structures in on-road calibration experiment.

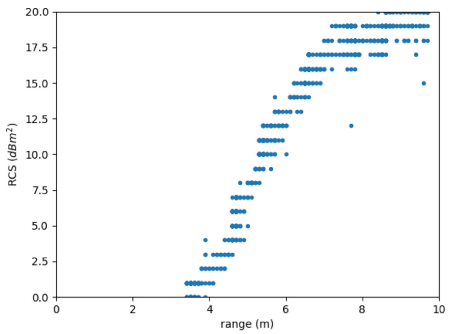

(a) Designed target

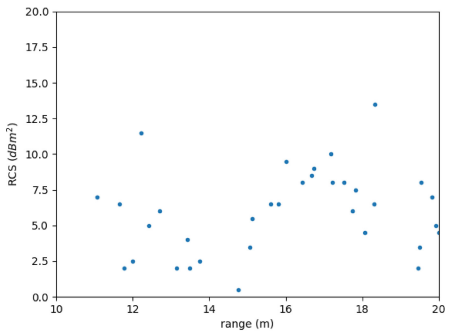

(b) Traffic light

FIGURE 17. The relationship between the RCS value and the target distance for designed target and traffic light.

traffic light's trajectory to reduce the disturbance from the metal pole.

There are twenty-two data logs located in Boston used for on-road calibration. Each log has over 1000 correspondences, and the result shows in Fig. 18. The mean errors of the estimated extrinsic parameters are under 0.08 meter and 0.03 degree compared to the benchmark from nuScenes. However, the variances of the estimated extrinsic parameters are under 0.14 meter and 0.23 degree which might be due to the interference on roads and that the uncertainties of measurements are larger than laboratory experiments. The results of the proposed method reach centimeter-level accuracy which proves it is feasible for on-road driving scenario.

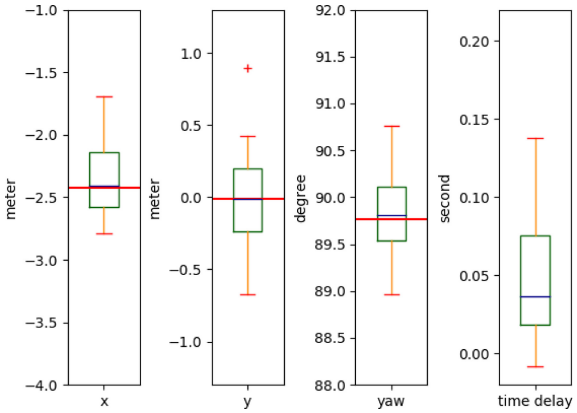

FIGURE 18. The result of on-road calibration. Red line: the benchmark offered from nuScenes; Box plot: the result estimated by proposed method.

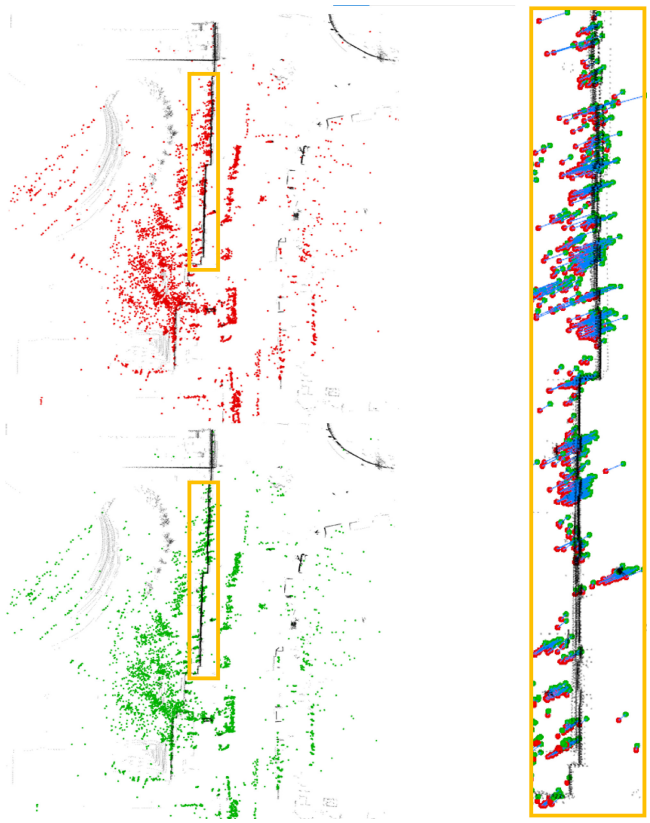

FIGURE 19. The comparison of radar map built before and after time delay compensation. Black point: LiDAR map; red point and green point: radar map built before and after time delay compensation; cyan line: the radar measurement correspondence before and after time delay compensation.

In addition, the foundational self-driving car tasks, mapping and object tracking, are used to demonstrate the effect of time delay compensation. With the offered poses, the radar measurements can be transformed and built to a radar map. With time delay compensation, the radar map is more concentrated and close to the LiDAR map as shown in Fig. 19. For object tracking, the time delay effects can be observed on nearby moving vehicles. The radar measurements without and with time delay compensation are compared with tracked target positions. Fig. 20 shows that a vehicle moves

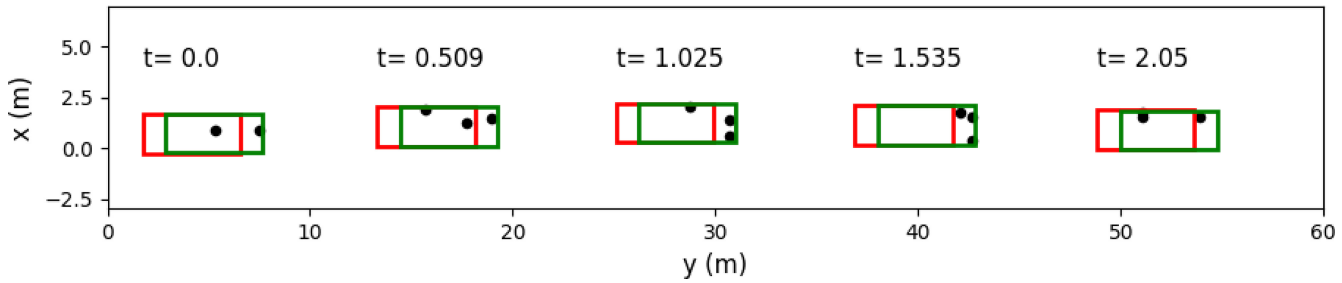

FIGURE 20. The comparison of moving object before and after time delay compensation. The object tracker frames the radar measurements more completely means radar and LiDAR become more consistent in time domain after time delay compensation. Black point: radar measurements; red and green frame: moving object label before and after time delay compensation.

at about 20 m/s, which cause about one meter compensation with 0.05 s estimated time delay. After time delay compensation, the radar measurements are more aligned with LiDAR measurements which shows the improvements from temporal calibration.

In summary, the performance of our on-road calibration procedure is confirmed. The 3 DoF extrinsic parameters are estimated and verified by benchmarking with the extrinsic parameters from nuScenes, and the improvement of time delay compensation is also evident.

VI. CONCLUSION

In this paper, we have presented a simultaneously extrinsic and temporal calibration approach for planar automotive radar and 3D-LiDAR using targets in factory settings and pre-selected objects in on-road settings. The feasibility and performance have been demonstrated using our collected datasets in factory calibration settings and nuScenes open datasets in on-road calibration settings.

For factory calibration settings, the proposed data collection procedure is demonstrated to significantly reduce the data collection effort and time and the six DoF extrinsic calibration and temporal calibration are accomplished. For on-road calibration settings, with the use of pre-labelled/pre-selected outdoor targets and their poses, the 3 DoF extrinsic parameters and time delay can be precisely estimated. It has been demonstrated that the extrinsic parameters reach centimeter-level accuracy, and time delay compensation improves the performance of radar tracking and mapping.

REFERENCES

[1] Y. H. Khalil and H. T. Mouftah, "LiCaNet: Further enhancement of joint perception and motion prediction based on multi-modal fusion," *IEEE Open J. Intell. Transp. Syst.*, vol. 3, pp. 222–235, 2022.

[2] F. Geissler, A. Unnervik, and M. Paulitsch, "A plausibility-based fault detection method for high-level fusion perception systems," *IEEE Open J. Intell. Transp. Syst.*, vol. 1, pp. 176–186, 2020.

[3] Z. Taylor and J. Nieto, "Motion-based calibration of multimodal sensor extrinsics and timing offset estimation," *IEEE Trans. Robot.*, vol. 32, no. 5, pp. 1215–1229, Oct. 2016.

[4] C. Park, P. Moghadam, S. Kim, S. Sridharan, and C. Fookes, "Spatiotemporal camera-LiDAR calibration: A targetless and structureless approach," *IEEE Robot. Autom. Lett.*, vol. 5, no. 2, pp. 1556–1563, Apr. 2020.

[5] W. Liu, "LiDAR-IMU time delay calibration based on iterative closest point and iterated sigma point Kalman filter," *Sensors*, vol. 17, no. 3, p. 539, 2017.

[6] F. M. Mirzaei and S. I. Roumeliotis, "A Kalman filter-based algorithm for IMU-camera calibration: Observability analysis and performance evaluation," *IEEE Trans. Robot.*, vol. 24, no. 5, pp. 1143–1156, Oct. 2008.

[7] M. Fleps, E. Mair, O. Ruepp, M. Suppa, and D. Burschka, "Optimization based IMU camera calibration," in *Proc. IEEE/RSJ Int. Conf. Intell. Robots Syst. (IROS)*, 2011, pp. 3297–3304.

[8] M. Li and A. I. Mourikis, "3-D motion estimation and online temporal calibration for camera-IMU systems," in *Proc. IEEE Int. Conf. Robot. Autom. (ICRA)*, 2013, pp. 5709–5716.

[9] J. Kelly and G. S. Sukhatme, "A general framework for temporal calibration of multiple proprioceptive and exteroceptive sensors," in *Experimental Robotics*. Berlin, Heidelberg, Germany: Springer, 2014, pp. 195–209.

[10] J. Kelly, N. Roy, and G. S. Sukhatme, "Determining the time delay between inertial and visual sensor measurements," *IEEE Trans. Robot.*, vol. 30, no. 6, pp. 1514–1523, Dec. 2014.

[11] J. Peršić, I. Marković, and I. Petrović, "Extrinsic 6Dof calibration of 3D LiDAR and radar," in *Proc. Eur. Conf. Mobile Robot. (ECMR)*, 2017, pp. 1–6.

[12] J. Peršić, I. Marković, and I. Petrović, "Extrinsic 6DoF calibration of a radar–LiDAR–camera system enhanced by radar cross section estimates evaluation," *Robot. Auton. Syst.*, vol. 114, pp. 217–230, Apr. 2019.

[13] H. Caesar et al., "nuScenes: A multimodal dataset for autonomous driving," 2019, *arXiv:1903.11027*.

[14] C.-L. Lee, Y.-H. Hsueh, C.-C. Wang, and W.-C. Lin, "Extrinsic and temporal calibration of automotive radar and 3D LiDAR," in *Proc. IEEE/RSJ Int. Conf. Intell. Robots Syst. (IROS)*, 2020, pp. 9976–9983.

[15] H. Zhang, D. Yang, E. Yurtsever, K. A. Redmill, and Ü. Özgüner, "Faraway-frustum: Dealing with LiDAR sparsity for 3D object detection using fusion," in *Proc. IEEE Int. Intell. Transp. Syst. Conf. (ITSC)*, 2021, pp. 2646–2652.

[16] T. Wang, N. Zheng, J. Xin, and Z. Ma, "Integrating millimeter wave radar with a monocular vision sensor for on-road obstacle detection applications," *Sensors*, vol. 11, no. 9, pp. 8992–9008, 2011.

[17] S. Sugimoto, H. Tateda, H. Takahashi, and M. Okutomi, "Obstacle detection using millimeter-wave radar and its visualization on image sequence," in *Proc. Int. Conf. Pattern Recognit. (ICPR)*, 2004, pp. 342–345.

[18] L. Heng, "Automatic targetless extrinsic calibration of multiple 3D LiDARs and radars," in *Proc. IEEE/RSJ Int. Conf. Intell. Robots Syst. (IROS)*, 2020, pp. 10669–10675.

[19] E. Wise, J. Peršić, C. Grebe, I. Petrović, and J. Kelly, "A continuous-time approach for 3D radar-to-camera extrinsic calibration," in *Proc. IEEE/RSJ Int. Conf. Robot. Autom. (ICRA)*, 2021, pp. 13164–13170.

[20] A. Geiger, F. Moosmann, Ö. Car, and B. Schuster, "Automatic camera and range sensor calibration using a single shot," in *Proc. IEEE Int. Conf. Robot. Autom. (ICRA)*, 2012, pp. 3936–3943.

[21] Y. Park, S. Yun, C. S. Won, K. Cho, K. Um, and S. Sim, "Calibration between color camera and 3D LIDAR instruments with a polygonal planar board," *Sensors*, vol. 14, no. 3, pp. 5333–5353, 2014.

[22] A. Dhall, K. Chelani, V. Radhakrishnan, and K. M. Krishna, "LiDAR-camera calibration using 3D-3D point correspondences," 2017, *arXiv:1705.09785*.

[23] C. Guindel, J. Beltrán, D. Martín, and F. García, "Automatic extrinsic calibration for LiDAR-stereo vehicle sensor setups," in *Proc. IEEE Int. Conf. Intell. Transp. Syst. (ITSC)*, 2017, pp. 1–6.
[24] J. Levinson and S. Thrun, "Automatic online calibration of cameras and lasers," in *Robot.: Sci. Syst. (RSS)*, vol. 2, no. 7, pp. 1–8, 2013.
[25] J. Castorena, U. S. Kamilov, and P. T. Boufounos, "Autocalibration of LiDAR and optical cameras via edge alignment," in *Proc. IEEE Int. Conf. Acoust. Speech Signal Process. (ICASSP)*, Mar. 2016, pp. 2862–2866.
[26] J. Jeong, L. Y. Cho, and A. Kim, "Road is enough! extrinsic calibration of non-overlapping stereo camera and LiDAR using road information," 2019, *arXiv:1902.10586*.
[27] C. Le Gentil, T. Vidal-Calleja, and S. Huang, "3D LiDAR-IMU calibration based on upsampled preintegrated measurements for motion distortion correction," in *Proc. IEEE Int. Conf. Robot. Autom. (ICRA)*, 2018, pp. 2149–2155.
[28] X. Yuwen et al., "Improved vehicle LiDAR calibration with trajectory-based hand-eye method," *IEEE Trans. Intell. Transp. Syst.*, vol. 23, no. 1, pp. 215–224, Jan. 2022.
[29] Z. Zhang, "Iterative point matching for registration of free-form curves and surfaces," *Int. J. Comput. Vis.*, vol. 13, no. 2, pp. 119–152, 1994.
[30] P. Biber and W. Straßer, "The normal distributions transform: A new approach to laser scan matching," in *Proc. IEEE/RSJ Int. Conf. Intell. Robots Syst. (IROS)*, vol. 3, 2003, pp. 2743–2748.
[31] E. Meijering, "A chronology of interpolation: From ancient astronomy to modern signal and image processing," *Proc. IEEE*, vol. 90, no. 3, pp. 319–342, Mar. 2002.
[32] S. Agarwal, K. Mierle, and The Ceres Solver Team, "Ceres solver." 2016. [Online]. Available: http://ceres-solver.org
[33] L. Stanislas and T. Peynot, "Characterisation of the delphi electronically scanning radar for robotics applications," in *Proc. Australas. Conf. Robot. Autom.*, 2015, pp. 1–10.

CHIA-LE LEE received the B.S. degree from National Chiao Tung University, Hsinchu, Taiwan, in 2019, and the M.S. degree from National Yang Ming Chiao Tung University, Hsinchu, in 2021. He is currently a Research and Development Engineer with Synopsys Inc. His research interests include robotics, machine learning, and machine perception.

CHUN-YU HOU received the B.S. degree from National Yang Ming Chiao Tung University, Hsinchu, Taiwan, in 2022, where he is currently pursuing the master's degree in electrical and computer engineering. His current research interests include robotics, machine learning, and machine perception.

CHIEH-CHIH (BOB) WANG received the B.S. and M.S. degrees from National Taiwan University, Taipei City, Taiwan, in 1994 and 1996, respectively, and the Ph.D. degree in robotics from the School of Computer Science, Carnegie Mellon University, Pittsburgh, PA, USA, in 2004. From 2004 to 2005, he was an Australian Research Council Research Fellow of the ARC Centre of Excellence for Autonomous Systems and the Australian Centre for Field Robotics with The University of Sydney, Sydney, Australia. From 2005 to 2015, he was with the Department of Computer Science and Information Engineering and the Graduate Institute of Networking and Multimedia, National Taiwan University. From 2015 to 2016, he worked with the Special Projects Group of Apple Inc. He is currently a Professor with the Department of Electrical and Computer Engineering, National Yang Ming Chiao Tung University, Hsinchu, Taiwan. His research interests include robotics, machine perception, and machine learning. He was a recipient of the Best Conference Paper Award at the 2003 IEEE International Conference on Robotics and Automation.

WEN-CHIEH LIN received the B.S. and M.S. degrees in control engineering from National Chiao Tung University (NCTU), Hsinchu, Taiwan, in 1994 and 1996, respectively, and the Ph.D. degree in robotics from the School of Computer Science, Carnegie Mellon University, Pittsburgh, in 2005. Since 2006, he has been with the Department of Computer Science, NCTU, where he served as the Director of the Institute of Multimedia Engineering from 2019 to 2022. He is currently a Professor with the Department of Computer Science, National Yang Ming Chiao Tung University, Taiwan. His research interests span several areas of computer graphics, human-computer interaction, and robotics.